# Supporting Information (SI)

## Triboelectric Nanogenerator Driven Self-Charging and Self-Healing Flexible Asymmetric Supercapacitor Power Cell for Direct Power Generation

***Anirban Maitra, Sarbaranjan Paria[#], Sumanta Kumar Karan[#], Ranadip Bera, Aswini Bera, Amit Kumar Das, Suman Kumar Si, Lopamudra Halder, Anurima De, and Bhanu Bhusan Khatua****

Materials Science Centre, Indian Institute of Technology Kharagpur, Kharagpur-721302, West Bengal, India.

# indicates equal contribution of the authors

***Corresponding Author**

Dr. B. B. Khatua (Email: *khatuabb@matsc.iitkgp.ernet.in*).

Materials Science Centre, Indian Institute of Technology, Kharagpur –721302, India.

Tel.:+91-3222-283982

**A. Materials Details.**

Cobalt (II) nitrate hexahydrate [$Co(NO_3)_2 \cdot 6H_2O$] (M.W.: 291.03 g/mole), iron (III) nitrate nonahydrate [$Fe(NO_3)_3 \cdot 9H_2O$] (M.W.: 404.0 g/mole), iron (III) chloride [$FeCl_3$] (M.W.: 162.2 g/mole), ammonium persulfate [$(NH_4)_2S_2O_8$] (M.W.: 228.18 g/mole), dimethylformamide [$C_3H_7NO$] (M.W.: 73.09 g/mole), ethylene glycol [$HOCH_2CH_2OH$] (M.W.: 62.0 g/mole) and hydrochloric acid (37%) were procured from Merck, Germany. Acrylic acid [$CH_2$=CHCOOH] (M.W.: 72.06 g/mole), ammonium hydroxide ($NH_4OH$) solution (28 %) and poly(vinylidene fluoride-co-hexafluoropropylene) ($M_w \approx 400{,}000.0$) were purchased from Sigma Aldrich. Potassium hydroxide flakes, isopropanol (M.W.: 60.10 g/mole), iron powder and graphite fine powder (98 %) were purchased from Loba Chemie Pvt. Ltd., India. Silver nanoparticles (AgNPs) (99.9 %, dia. ~ 30 nm) were obtained from Alfa Aesar Pvt. Ltd. India. Liquid polydimethylsiloxane [PDMS] elastomer (Sylgard 184) and its curing agent were obtained from Dow Corning Corp., USA. Carboxylated polyurethane (CPU) was purchased from Wanhua Chemical Group Co., Ltd. Graphite sheet (sheet thickness ~ 0.25 cm) was purchased from Nickunj Eximp Entp Pvt. Ltd., India. Commercially available stainless steel (SS) fabric with an average pore diameter ~ 110 μm was exploited as conductive substrates as well as electrodes in the SHASC and the HPTENG devices. Prior to utilize, all the SS fabrics were mirror polished with a piece of emery paper followed by washing with de-ionized (DI) water and ethanol for several times and dried at 40 ºC for ~ 24 h. Commercially available medical syringe (DISPO VAN/2 mL), cigarette wrapper, transparent PP sheets (thickness ≈ 0.11 mm), adhesive and PP tapes (d ≈ 0.04 mm) were purchased from the local market. DI water with a resistivity value of ~ 18 MΩ-cm acquired from a JL–RO100 Millipore–Q Plus water purifier was used in the experiments.

**B. Preparation of the asymmetric supercapacitor (ASC) components:**

***B1. Preparation of positive and negative component electrodes ($CoFe_2O_4$@SS and Fe-RGO@SS):***

$CoFe_2O_4$@SS electrode was prepared by direct growth/deposition of magnetic $CoFe_2O_4$ on a polished SS fabric substrate (current collector) through a cathodic electrodeposition followed by an annealing treatment. A piece of SS fabric (2×2 $cm^2$) was first polished and washed thoroughly with water/ethanol for several times. Thereafter, the electrodeposition was executed at room temperature with a mixed electrolyte employing conventional three-electrode configuration. The electrolyte comprises a mixture of 0.1 M $Co(NO_3)_2$•$6H_2O$ and 0.2 M $Fe(NO_3)_3$•$9H_2O$ in ethylene glycol. During electrodeposition, the SS fabric was employed as working electrode while a graphite sheet (2×2 $cm^2$) and a saturated calomel electrode (SCE) was used as counter and reference electrode, accordingly. The working and counter electrode were placed at a distance of 0.8 cm while the applied current density was 2 mA/$cm^2$. After 30 min of electrodeposition, the electrodeposited SS fabric was gently removed, washed with DI water, ethanol and kept in an air oven at ~ 60 ºC for drying. Afterwards, the dried electrode ($CoFe_2$ alloy electrodeposited on SS) was annealed in presence of air at 500 ºC for ~ 5 h to convert $CoFe_2$ alloy into $CoFe_2O_4$.[1, 2] Subsequently, a homogeneous dispersion of silver nanoparticles (Ag NPs) in isopropanol solvent (1 mg/mL) was slowly drop casted (4 μL) on the as-fabricated electrode and dried at ~ 55 ºC for 8 h. Introducing trace AgNPs eventually enhances the charge transport properties of the electrode material.[3, 4] Finally, the as-prepared electrode was marked as $CoFe_2O_4$@SS and employed as binder-free positive electrode in the SHASC device. The mass of $CoFe_2O_4$ deposited on SS fabric was ~ 0.026 g (6.5 mg/$cm^2$). Contrariwise, magnetic Fe-RGO@SS was prepared by depositing Fe-RGO on polished SS fabric substrate. Initially, a piece of SS fabric substrate (2×2 $cm^2$) was kept immersed in graphene oxide (GO) suspension for ~ 24 h. The GO suspension was prepared by uniformly dispersing 0.3 g of GO (synthesized by employing the modified Hummers' method from graphite powder)[5] in 100 mL DI water by ultrasonication for 50 min. After 24 h of SS immersion, ~ 0.17 g pure iron (Fe) powder (avg.

particle size 10 μm) and 25 mL HCl (37 wt %) were added gradually to the above suspension at room temperature under stirring condition. After proper mixing, the suspension was continuously stirred for ~ 30 h to reduce GO at room temperature. After the reduction, excess HCl was added in dropwise manner to oxidize superfluous Fe powder.[6] Afterwards, 28 % ammonium hydroxide solution was added gently under slow stirring (at pH ≈ 10) and kept for ~ 10 h (under stirring condition) and additional 6 h (without stirring). During reaction, both the $Fe(OH)_3$ and $Fe(OH)_2$ were formed which eventually dehydrated to $Fe_3O_4$ with a small extent of $Fe_2O_3$.[7-9] Finally, iron oxides decorated RGO deposited on the SS fabric substrate was gently removed, washed with DI water, ethanol and kept in air oven at 80 ºC for drying. This electrode was marked as Fe-RGO@SS and employed as binder-free negative electrode in SHASC device. The mass of Fe-RGO deposited on SS was 0.048 g (12 mg/cm$^2$).

***B2. Preparation of a KOH soaked self-healing polymer hydrogel electrolyte membrane/separator ($Fe^{3+}$–PAA/KOH):*** Primarily, the self-healing polymer hydrogel membrane/separator was prepared by employing typical free radical polymerization technique followed by ionic crosslinking in between polyacrylic acid (PAA) chains and $Fe^{3+}$ ions.[10] At the onset, 6 mole% of $FeCl_3$ (with respect to the monomer) was added to an aqueous acrylic acid solution. The ultimate solution was vigorously stirred for ~ 30 min at room temperature. Afterwards, ammonium persulfate initiator (~ 1 wt% of acrylic acid) was gently added into the above mixture in presence of argon atmosphere and subsequently heated at ~ 50 ºC. After few minutes, the entire solution turned highly viscous (pre-gel state). It was then slowly casted on a Petri dish and kept at ~ 50 ºC in a vacuum oven for 14 h for complete gelation. Finally, the hydrogel membrane (thickness ≈ 1.2 mm) was slowly peeled off from the Petri dish and washed with DI water. This self-healing hydrogel membrane ($Fe^{3+}$–PAA) was kept immersed in aqueous 1 M KOH solution for ~ 18 min to obtain $Fe^{3+}$–PAA/KOH hydrogel electrolyte separator for the SHASC device.

**C. Materials characterization.**

X–ray diffraction (XRD) patterns of the as-deposited SS fabric electrodes were executed by mounting the electrodes on X Pert PRO diffractometer [PANalytical, Netherland] with a monochromatic Cu $K_\alpha$ radiation ($\lambda$=0.15418 nm). X–ray photoelectron spectroscopic studies were accomplished by utilizing a PHI 5000 Versa Probe II type spectrometer [having Al $K_\alpha$ source ~ 1486 eV].[11] Before performing the XPS analysis, the as-deposited Fe-RGO were gently peeled off/scratched from SS substrates and then loaded on the XPS instrument in pellet forms. The typical survey scan spectrum was acquired with reference to aliphatic carbon having a binding energy of ~ 284.1 eV. The weigh amount of RGO and iron oxides in Fe-RGO have been estimated by utilizing a TGA-Q50 (TA instruments), USA within a wide temperature range starting from room temperature (25 °C) to 800 °C at a heating rate of 10 °C $min^{-1}$ under continuous air flow. Field emission scanning electron microscopic (FE–SEM) analyses were executed by employing a Carl Zeiss–SUPRA 40 (Oberkochen, Germany) within 5 kV operating voltage. The corresponding energy dispersive X–ray line spectrums (EDX) and elemental mappings were obtained from an energy dispersive spectrometer (EDS) attached with the FE–SEM unit. Fourier Transformed Infrared spectroscopic analyses were executed (utilizing NEXUS–870, Thermo Nicolet) within 4000 – 400 $cm^{-1}$. Raman spectra of the electroactive materials were acquired from a Raman triple spectrometer (model T–64000, HORIBA Jobin Yvon, France). Electrochemical measurements of as-prepared $CoFe_2O_4$@SS and Fe-RGO@SS were executed by using a three-electrode cell configuration on a Biologic SP–150 electrochemical work station. In conventional three-electrode configuration, $CoFe_2O_4$@SS and Fe-RGO@SS (2×2 $cm^2$) electrodes were utilized as working electrode individually, while a platinum (Pt) foil (1×1 $cm^2$) and a saturated calomel electrode (SCE) were employed as counter and reference electrode, accordingly. The entire electrochemical measurements of the assembled SHASC was accomplished by employing a two-electrode cell configuration with $CoFe_2O_4$@SS as positive and Fe-RGO@SS as negative electrodes separated by a

KOH soaked $Fe^{3+}$–PAA self-healing hydrogel electrolyte membrane/separator. All the electrochemical impedance spectroscopic (EIS) analyses were executed within 1 MHz – 100 mHz frequency range with 10 mV AC voltage amplitude. The magnetic response of $CoFe_2O_4$ and Fe-RGO were executed by employing a vibrating sample magnetometer (Lake Shore cryotronics, USA: model 7400) within an applied field of ± 16 kOe at room temperature. Before performing the VSM measurements, the electrode materials were peeled-off from SS substrate and loaded on the instrument. Mechanical properties of $Fe^{3+}$–PAA/KOH hydrogel electrolyte separator and CPU film (encapsulator) were analyzed by employing ZwickRoell tensile testing system with a stretching speed of 50 mm/min. The swelling behavior of the hydrogel separator was perceived by dipping the membrane in 1 M KOH for ~ 33 min.[10] The output voltages ($V_O$) of the TENG and HPTENGs were evaluated by utilizing a digital oscilloscope (ROHDE & SCHWARZ, RTM–2022) with an input impedance of 1 MΩ. The short circuit current ($I_{SC}$) of the TENG and HPTENGs were evaluated by using a Keithley–4220 electrometer. Self-charge/discharge performance of the SCSHASC power cell was inspected by employing Biologic SP–150 electrochemical work station with a two-electrode cell set-up. The $V_O$ attained by SCSHASC during practical application was monitored by using a commercial multimeter (FLUKE 115 true RMS).

**D. Utilized equations:**

The charge (q) of the component electrodes and the optimized mass ratio ($m_+/m_-$) amongst the two electroactive materials deposited on SS was calculated by employing the following equations:[3, 12]

$$q = C \times \Delta V \times m \qquad \text{(E1)}$$

$$\frac{m_+}{m_-} = \frac{C_- \times \Delta V_-}{C_+ \times \Delta V_+} \qquad \text{(E2)}$$

Here, C, ΔV and m denotes the specific capacitance (in F/g), operating voltage window (V) and mass of the active electrode materials (g). Additionally, the $C_{sp,}$ $C_s$ and $C_A$ of individual electrode materials and the SHASC device was assessed from their relevant GCD profiles using the following equations:[13]

$$C_{sp} = \frac{i \times \Delta t}{m \times \Delta V} \qquad \text{(E3)}$$

$$C_s = \mathrm{C}_{sp}/\Delta\mathrm{V} \qquad \text{(E3a)}$$

$$C_A = \frac{i \times \Delta t}{A \times \Delta V} \qquad \text{(E4)}$$

Here, $C_{sp}$, $C_s$ and $C_A$ are the specific capacitance (F/g), specific capacity (mAh/g) and areal capacitance (F/cm$^2$), accordingly. (i/m) and (i/A) indicates the current density (A/g) and areal current density (A/cm$^2$), accordingly. ΔV is the potential drop (V) while discharging and Δt symbolizes the time (s) for frequent discharging. The energy and the power density of the SHASC was calculated by utilizing the following equations:[14]

$$E_{SHASC} = \frac{1}{2} \times C_{SHASC} \times (\Delta V)^2 \qquad \text{(E5)}$$

$$P_{SHASC} = E_{SHASC} / T \qquad \text{(E6)}$$

Here, $E_{SHASC}$ and $P_{SHASC}$ symbolize energy density (in Wh/Kg) and the power density (in W/Kg) of the SHASC, accordingly. $C_{SHASC}$ denotes the specific capacitance (in F/g); ΔV is the voltage window (V); T symbolizes the discharging time of the SHASC, respectively.

The % swelling ratio (SR) of the hydrogel membrane/separator (in 1 M KOH) was calculated by using the following equation:[10]

$$SR(\%) = \frac{W_f - W_i}{W_i} \times 100 \qquad \text{(E7)}$$

Here, $W_i$ and $W_f$ represents the initial weight (g) of the hydrogel membrane and weight after consequent swelling at a particular time, accordingly. Moreover, the force applied during periodic finger imparting was calculated by employing the kinetic energy and momentum theory. The used equations are:[15-17]

$$m.g.h = \frac{1}{2} \times m \times V^2 \qquad \text{(E8)}$$

$$(F - mg) \times \Delta t = mV \qquad \text{(E9)}$$

$$\sigma = \frac{F}{Area} \qquad \text{(E10)}$$

Where m represents the average mass of the tapping body/limbs, *h* represents the particular height of falling; V symbolizes the average velocity of falling; *F* and $\Delta t$ represents the average contact force during imparting and the time span, respectively. Here, we have considered m ≈ 1.20 kg, g = 9.8 N/kg, area = 0.0024 $m^2$, h ≈ 0.11 m, and Δt ≈ 0.30 s. Thus, the calculated applied force (*F*) and the contact pressure (σ) generated during finger imparting were ≈ 17.6 N and 7.34 KPa, respectively. Further, the instant output power/power density of a single HPTENG was calculated by utilizing the following equation:[18]

$$P = \frac{V^2}{R_L \times Area} \qquad \text{(E11)}$$

Here, P represents the power density of HPTENG (μW/$cm^2$), V denotes the maximum output voltage (in V) generated from the HPTENG at a load resistance $R_L$ (Ω). The surface charge density ($Q_D$) was calculated from their own current *vs*. time curves with the help of the following equation:

$$Q_D = \frac{\int i \times t}{Area} \qquad \text{(E12)}$$

The numerator of this equation implies the integral area of current *vs*. time curve at a certain time span.

**E. XPS and TGA analysis of Fe-RGO:**

The narrow scan XPS profiles of Fe-RGO have been illustrated in Figure S1(a–c). As shown in Figure S1a, the Fe 2p spectrum consist two characteristic peaks centered at a binding energy of ~ 710.4 eV and 724.8 eV resembles to Fe $2p_{3/2}$ and Fe $2p_{1/2}$ peaks of $Fe_3O_4$, accordingly.[19] In addition, a small shakeup satellite peak centered at a binding energy of 719.0 eV signifying minute existence of $Fe_2O_3$

phase.[20, 21] As revealed in Figure S1b, the characteristic Fe $2p_{3/2}$ spectrum can be split into two peaks centered at a binding energy ~ 710.0 eV and 710.7 eV, ascribed to the existence of both $Fe^{2+}$ and $Fe^{3+}$, accordingly. Besides, the acquired O1s spectrum of Fe-RGO can be split into three peaks centered at a binding energy of ~ 529.2 eV, 530.0 eV and 530.9 eV after deconvolution (as shown in Figure S1c). These characteristic peaks ascribed to different chemical environments. The peak at 530.0 eV evidently illustrates the presence of oxygen in "oxide" form whereas the peak at 530.9 eV arises possibly owing to the minute existence of C–OH.[22, 23] Minor amount of Fe–OOH (impurity) can be identified from the spectrum (~ 529.2 eV). All these acquired signatures eventually illustrate the presence of mixed iron oxides (solely $Fe_3O_4$ with trace quantity of $Fe_2O_3$) in Fe-RGO. Moreover, Thermogravimetric analysis (TGA) has been employed to estimate the weigh amount of RGO and iron oxides in Fe-RGO (Figure S1d). The TGA profiles of RGO (black) and Fe-RGO (red) follows two-step degradation in air. It has been perceived that weigh amount of RGO and mixed iron oxides in Fe-RGO (initial wt. loading = 9.758 mg ≈ 100 %) were 4.6834 mg (48 %) and 5.0741 mg (52 %).

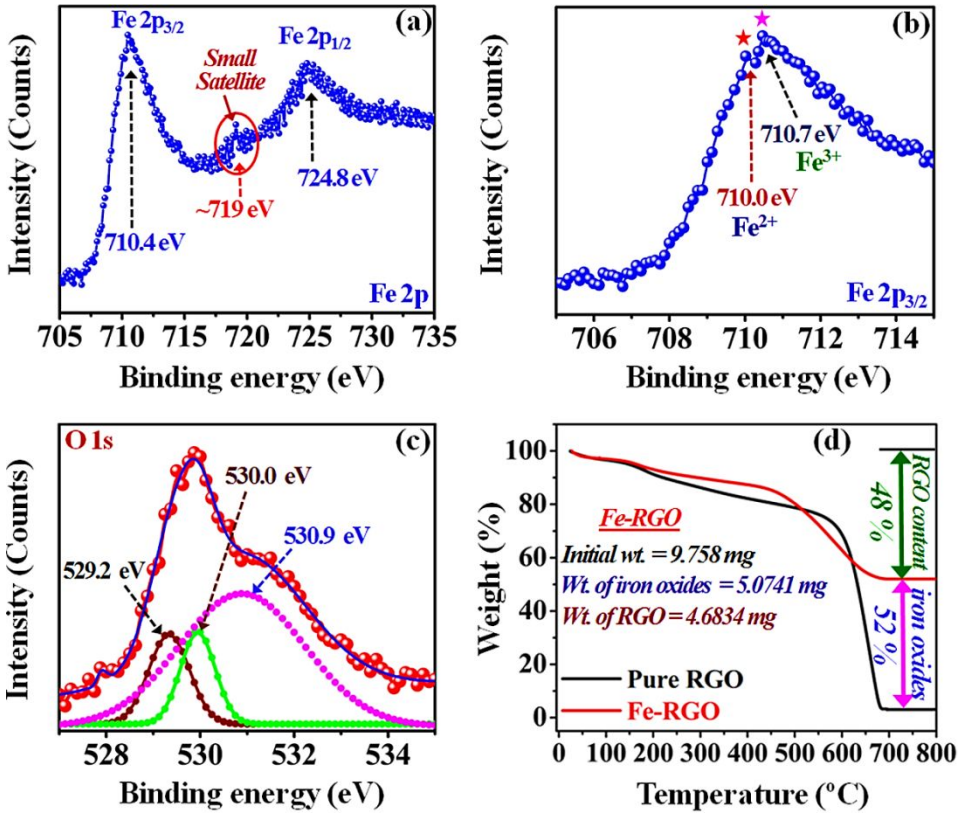

**Figure S1.** Narrow scan profiles of Fe-RGO: (a) Fe 2p, (b) Fe $2p_{3/2}$, and (c) deconvoluted O 1s. (d) TGA plots of RGO (pure/pristine) and as-prepared Fe-RGO in air.

**F. Elemental mappings and EDS patterns of both $CoFe_2O_4$ and Fe-RGO:**

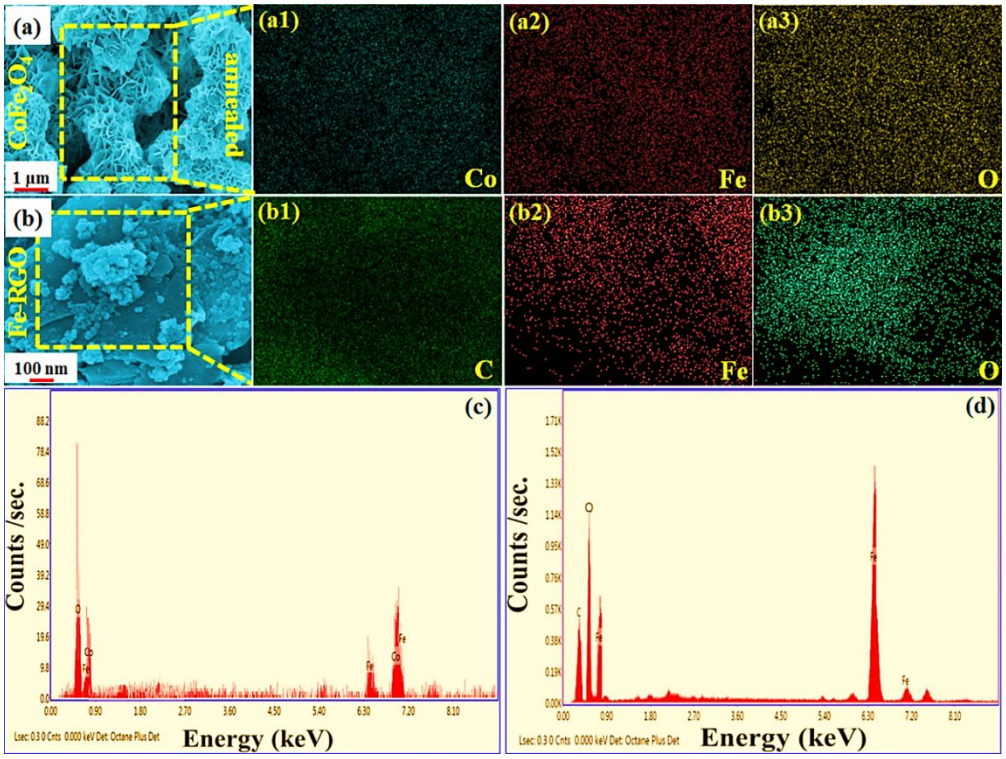


**Figure S2.** (a, b) Selected areas for elemental mapping of $CoFe_2O_4$ and Fe-RGO, respectively. (a1–a3) displays the co-existence of Co, Fe, and O in $CoFe_2O_4$, individually. (b1–b3) displays the co-existence of C, Fe, and O, individually in Fe-RGO. (c, d) EDS pattern of $CoFe_2O_4$ and Fe-RGO, consequently.

**G. Morphologies of $CoFe_2O_4$@SS and Fe-RGO@SS after completion of 8000 successive GCD cycles and after several finger imparting/tapping cycles:**

To comprehend the effect of rapid electrolyte diffusion and fast surface redox reactions on the microstructures of the component electrodes during repetitive cycling, the FE-SEM analysis has been executed after the completion of 8000 consecutive GCD cycles and numerous finger imparting/tapping cycles. Figure S3a, b represents the morphological features of the $CoFe_2O_4$@SS (+ Ve electrode) after 8000 GCD cycles. As revealed in Figure S3a, the interconnected microflowers-like arrays still persists

even after long-term/vigorous cycling. Figure S3b displays that the microflowers contain numerous ultrathin nanopetals with marginally increased thickness (~ 20–24 nm) and faintly broken edges. This increase in thickness probably attributed to the swelling of the nanopetals by electrolyte.[22] Likewise, the internal cavities are well-preserved after vigorous GCD cycles. Figure S3d, e depicts the acquired morphological features of the Fe-RGO@SS (–Ve electrode) after 8000 GCD cycles. Typical flake-like architecture of RGO decorated with iron oxides still persists after long-term electrochemical cycling. The retention of this flake-like morphology offers a large specific surface area for enhanced electrode-electrolyte interactions. The thickness of the RGO nanoflake becomes ~ 25–28 nm owing to swelling effect. These outcomes essentially illustrate the microstructural stability of the component electrodes against long-term cycling. Furthermore, the durability of these microstructures against repetitive finger imparting/tapping cycles is demonstrated in Figure S3c and f. It has been realized, the microflowers of $CoFe_2O_4$ (Figure S3c) and flake-like architecture of Fe-RGO (Figure S3f) still sustains after long and repetitive imparting cycles. The justifications behind the microstructural stability of $CoFe_2O_4$@SS and Fe-RGO@SS electrodes after repetitive imparting are: (i) both the microstructures inherently restrict deformations (micro to nano level) upon application of stress; (ii) in the ultimate device, the electrodes are surrounded by two elastomeric PDMS flip-strip which restricts the electrodes from abrupt shocks; (iii) owing to inherently high load bearing ability of SS, it absorbs impact/shocks from both sides during long and repetitive imparting cycles; (iv) CPU encapsulation also protects the components and microstructures from vigorous mechanical damage; (e) direct growth/deposition of the active materials on polished SS fabric substrates might be another feasible reason for the adequate structural stability.

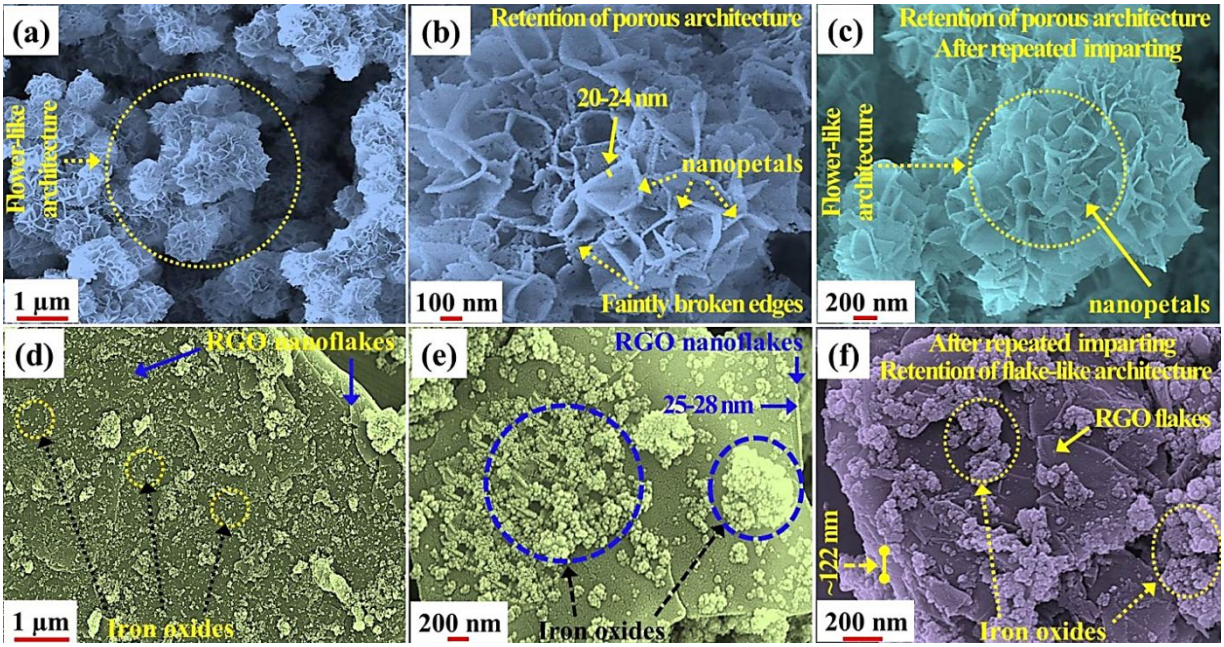


**Figure S3.** FE–SEM images of (a, b) $CoFe_2O_4$@SS, (d, e) Fe-RGO@SS (at different magnifications) after 8000 GCD cycles. (c, f) $CoFe_2O_4$@SS and Fe-RGO@SS acquired after several imparting cycles, accordingly.

**H. Fourier Transformed Infrared (FTIR) and Raman spectroscopic analysis:**

To determine the bond information and structural features of the as-synthesized electroactive materials, FTIR spectroscopic analysis has been executed. Figure S4a reveals the FTIR spectrum of $CoFe_2O_4$. Two characteristic peaks appeared at *ca.* 574 $cm^{-1}$ and 460 $cm^{-1}$ signifies the existence of typical $Fe^{3+}$–$O^{2-}$ bond.[24] These typical signatures are observed in almost all the ferrite materials. Additionally, two characteristic peaks appeared at *ca.* 1614 $cm^{-1}$ and 1399 $cm^{-1}$ is attributed to the antisymetric and symmetric stretching of cobalt metals, accordingly. A broad peak appeared at *ca.* 3420 $cm^{-1}$ is owing to the presence of O–H stretching vibrations of adsorbed water molecules.[25] Figure S4b represents the FTIR spectrum of GO and Fe-RGO. The FT–IR spectrum of GO (synthesized by modified Hummers' method) consists of seven moderate to low intensity peaks at *ca.* 1102 $cm^{-1}$ for alkoxyl C–O groups, 1238 $cm^{-1}$ for epoxy C–O groups, 1422 $cm^{-1}$ for carboxyl C–O stretching vibration, 1572 $cm^{-1}$ for aromatic C=C, 1716 $cm^{-1}$ for C=O stretching vibration, 2920 $cm^{-1}$ possibly for H–O–H stretching

vibration and 3430 $cm^{-1}$ for hydroxyl group stretching vibrations. The FT–IR spectrum of Fe-RGO (blue curve) consists of six characteristic peaks. Three of them appeared at 1403 $cm^{-1}$ for carboxyl C–O stretching vibration, 1541 $cm^{-1}$ for aromatic C=C and 3280 $cm^{-1}$ for hydroxyl stretching vibrations. The other three peaks appeared at *ca.* 628 $cm^{-1}$ for bulk magnetite, 555 $cm^{-1}$ and 455 $cm^{-1}$ signifies the existence of $Fe^{3+}$–$O^{2-}$ bond.[26-28] The absence of other characteristic peaks of GO in Fe-RGO suggests proper reduction of GO where Fe-powder used as reducing agent. The spectrum likewise illustrates the formation of mixed iron oxides (solely $Fe_3O_4$ with trace quantity of $Fe_2O_3$) in RGO. Figure S4c reveals the Raman spectrum of $CoFe_2O_4$ where four moderate to low intensity bands has been recognized at *ca.* 698 $cm^{-1}$ (for $A_{1g}$), 611 $cm^{-1}$(for $A_{1g}$), 560.5 $cm^{-1}$ ($T_{2g}$) and 484 $cm^{-1}$ ($T_{2g}$). The acquired Raman active modes eventually illustrate the formation of cobalt ferrite with spinal structure. It is to be stated that no other distinctive Raman active bands are observed for $Fe_2O_3$/$Fe_3O_4$ (impurity) in $CoFe_2O_4$.[29] Figure S4d represents the acquired Raman spectrum of Fe-RGO where the two characteristic Raman active bands at *ca.* 1363 $cm^{-1}$ (signature of D band) and 1585 $cm^{-1}$ (signature of G band) have been recognized. The characteristic D band appears owing to the existence of $sp^3$ defects while the G band reveals in-plane vibration of $sp^2$ hybridized carbon in RGO. The $I_D/I_G$ ratio becomes ~ 1.09 signifying higher defects generated in RGO (as compared to GO) due to the existence of iron oxides. Moreover, a high intensity band at *ca.* 682 $cm^{-1}$ signifies the presence of $Fe_3O_4$ while two small bands at *ca.* 518 $cm^{-1}$ and 581 $cm^{-1}$ suggest the existence of minute $Fe_2O_3$ in Fe-RGO.[30-32] Hence, it can be inferred that both $CoFe_2O_4$ (spinel) and Fe-RGO has been formed successfully on SS fabric substrates.

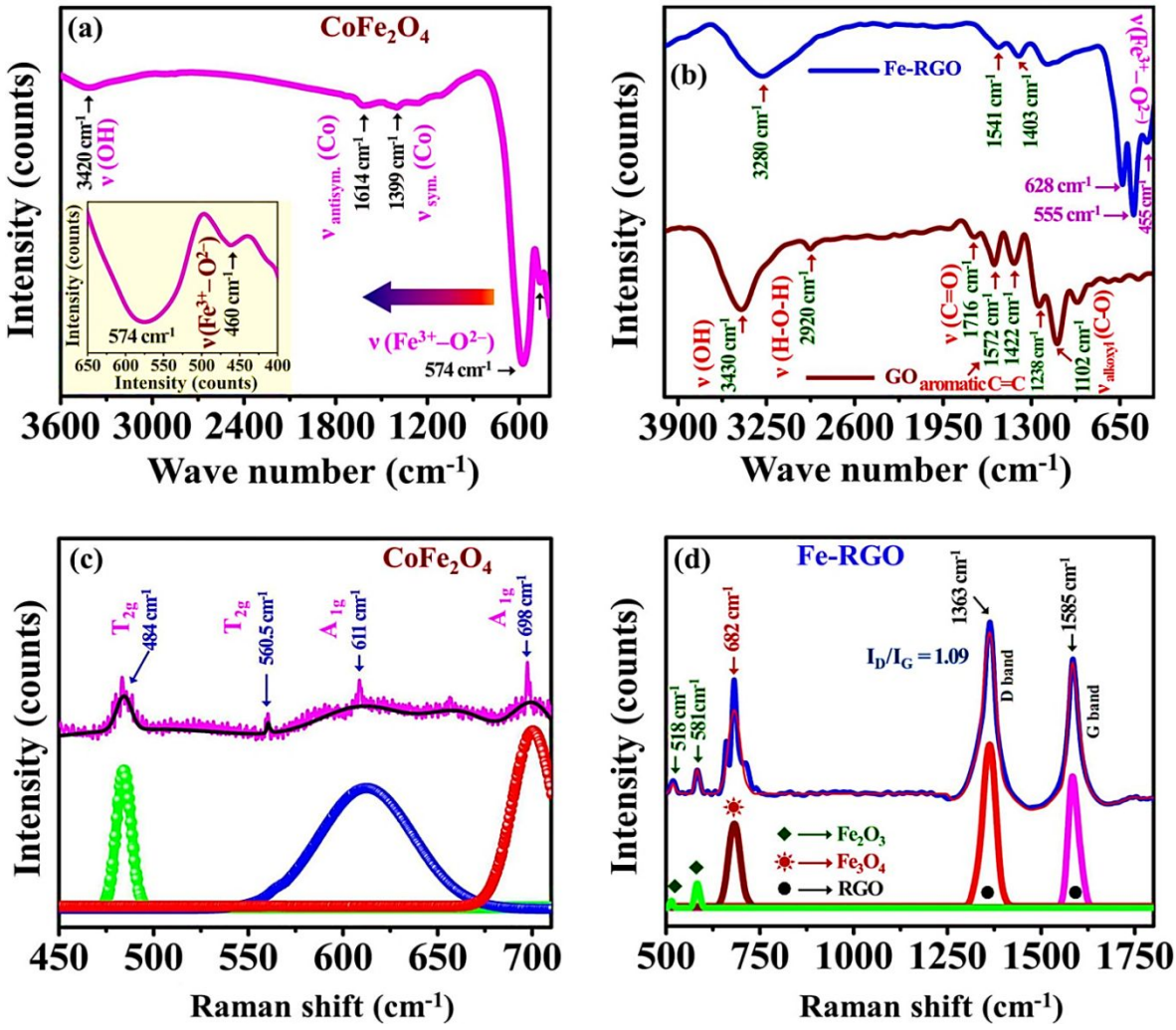


**Figure S4.** (a) FTIR spectrum of $CoFe_2O_4$. (b) Comparison of the FTIR spectra of GO and Fe-RGO. Deconvoluted Raman spectrum of (c) $CoFe_2O_4$ and (d) Fe-RGO.

**I. Complete electrochemical analysis of $CoFe_2O_4$@SS (positive electrode):**

Prior to assemble the SHASC device, comprehensive electrochemical analysis of $CoFe_2O_4$@SS has been executed utilizing a conventional three-electrode cell set-up within 0–0.6 V potential window in presence of aqueous 1 M KOH electrolyte. Before the execution of CV, GCD and EIS analyses, all the electrode materials were frequently charged and discharged at a current density of 5 A/g for ~ 50 GCD cycles until a stable $C_{sp}$ value attains. Afterwards, the electrochemical analyses have been executed. As mentioned earlier, trace Ag NPs was introduced in $CoFe_2O_4$@SS electrode to enhance the charge

transport kinetics. Figure S5a shows the acquired CV profiles of $CoFe_2O_4$@SS (Ag NPs incorporated) at several scan rates of 2, 5, 10, 30, 50, 80, 100, 120, and 150 mV/s, individually. All the CV profiles exhibits a pair of redox peaks within 0–0.6 V attributed to the following reactions:[33]

$$CoFe_2O_4 + H_2O + OH^- \leftrightarrow CoOOH + 2\ FeOOH + e^- \quad \text{(I)}$$

$$CoOOH + OH^- \leftrightarrow CoO_2 + H_2O + e^- \quad \text{(II)}$$

$$FeOOH + H_2O \leftrightarrow Fe(OH)_3 \leftrightarrow (FeO_4)^{2-} + 3e^- \quad \text{(III)}$$

The anodic peak (broad) appears at ~ 0.50 V while the cathodic peak appears at ~ 0.35 V. A minor shifting of the peak voltage positions with the elevation of scan rate can be attributed to composition "polarization". Likewise, upon elevating the scan rate, the current response increases suggesting an enhanced diffusion of the electrolytic ions inside the cavities of the electroactive materials. Besides, incorporating Ag NPs into $CoFe_2O_4$@SS eventually improves its capacitive response and conductivity. As can be seen in Figure S5b, the CV curves of $CoFe_2O_4$@SS (with Ag NPs) exhibit a higher area than $CoFe_2O_4$@SS (without Ag NPs). Figure S5c compares the CV of $CoFe_2O_4$@SS (Ag NPs incorporated) and blank SS to elucidate the capacitance contribution of blank SS fabric (if any). It is apparent that the contribution of blank SS fabric is negligible as compared to $CoFe_2O_4$@SS (with Ag NPs) electrode. The GCD profiles of $CoFe_2O_4$@SS (Ag NPs incorporated) are demonstrated in Figure S5d at a varying current density of 1, 2, 3, 5, 8, 10, 15 and 20 A/g within 0–0.6 V potential window. All the profiles illustrate Faradaic behavior of the electrode with a tiny plateau region. The as-prepared $CoFe_2O_4$@SS (Ag NPs incorporated) reveals a $C_{sp}$ value of ~ 1055.0 F/g ($C_s \approx$ 175.84 mAh/g) at 1 A/g and a $C_A$ of ~ 6850 mF/cm$^2$ at 6.5 mA/cm$^2$ current density (calculated by employing equation E3, E3a and E4, accordingly). The actual mass of $CoFe_2O_4$ was ~ 0.026 g. The $C_{sp}$ still retains up to ~ 970.6 F/g ($C_s \approx$ 161.77 mAh/g) at a high current density of 20 A/g signifying admirable rate capability of the electrode. Figure S5e compares the acquired GCD profiles of $CoFe_2O_4$@SS (with Ag NPs) and $CoFe_2O_4$@SS (without Ag NPs). It has been recognized that $CoFe_2O_4$@SS (without Ag NPs) exhibits a maximum

$C_{sp}$ of ~ 978.6 F/g at 1 A/g which is fairly lower than that of $CoFe_2O_4$@SS (with Ag NPs). Hence, this Ag NPs incorporated $CoFe_2O_4$@SS was employed as positive electrode in the SHASC. Figure S5f shows the variation of gravimetric $C_{sp}$ with the applied current density. A gentle diminution in the $C_{sp}$ has been observed with the increment of current density owing to less availability of the redox active sights for Faradaic reactions especially at higher current densities. The inset demonstrates the magnetic healing behavior of $CoFe_2O_4$@SS. As can be realized, the shape of the GCD curve remains equivalent after healing through magnetic attraction. Figure S5g illustrates the variation of $C_A$ with areal current density. In a similar way, a diminution in the $C_A$ values has been observed with the increment of areal current density. The $C_A$ value still retains up to ~ 6300 mF/cm$^2$ even at 130 mA/cm$^2$ high areal current density. Figure S5h exhibits the Nyquist plots or complex plane impedance profiles: initially and after 5000 GCD cycles. The shapes of the impedance profiles are analogous. Each profile comprises a semicircular arc at high-frequency region followed by a steeper line at low-frequency region. Initially, the electrode exhibits an $R_{ct}$ of ~ 1.6 Ω which is smaller than ~ 1.92 Ω (after 5000 cycle). Moreover, the initial impedance profile displays a more vertical line (having a higher slope) at low frequency in comparison to the impedance profile after 5000 GCD cycles. The low $R_{ct}$ of $CoFe_2O_4$@SS suggests better reactivity, faster electrolyte ion transport kinetics. The equivalent circuit diagram fitted to the Nyquist plot is shown in the inset. The GCD cyclic stability measurement of the electrode has been accomplished at 1 A/g constant current density for 5000 cycles within 0–0.6 V (as displayed in Figure S5i). The interconnected microflowers obstruct the volume expansion during vigorous cycling. As a result, it exhibits long-term stability against repetitive electrochemical cycling with 94.4 % of its initial $C_{sp}$ retention after 5000 GCD cycles. A moderate increment of $C_{sp}$ (~ 2.8 %) during few initial GCD cycles can be attributed to time-dependent diffusion of the electrolytic ions through the pores/cavities of $CoFe_2O_4$ microflowers. This phenomenon suggests complete utilization of the electrode surface after few charge/discharge cycles. The first 10 GCD cycles (at 1 A/g) is displayed in the inset.

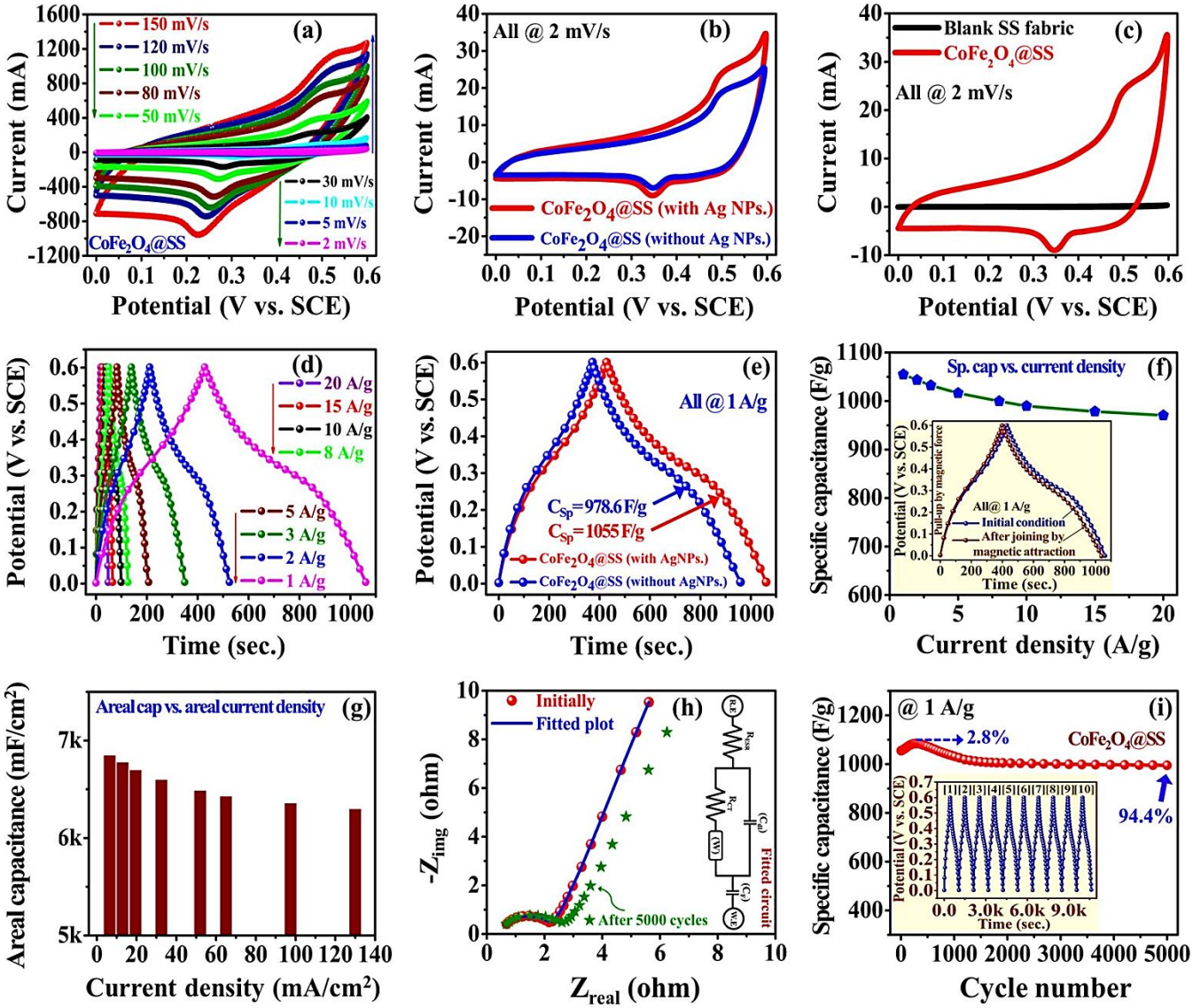


**Figure S5.** (a) CV curves of $CoFe_2O_4$@SS electrodes at various scan rates. (b) A comparison between the CV curves of $CoFe_2O_4$@SS (with Ag NPs) and $CoFe_2O_4$@SS (without Ag NPs) at 2 mV/s. (c) A comparison between the CV curves of $CoFe_2O_4$@SS and blank SS fabric at 2 mV/s. (d) GCD curves at various current densities. (e) A comparison between the GCD curves of $CoFe_2O_4$@SS (with Ag NPs) and $CoFe_2O_4$@SS (without Ag NPs) at 1 A/g. (f) Variation of $C_{sp}$ values with current densities. (Inset demonstrates the GCD curves of $CoFe_2O_4$@SS at 1 A/g; before cutting and after joining by magnetic attraction). (g) Variation of $C_A$ with the areal current density. (h) Nyquist plot: initially and after 5000 GCD cycles. (Inset denotes the fitted circuit diagram). (i) $C_{sp}$ retention after 5000 GCD cycles at 1 A/g. (Inset depicts the sequential GCD profile up to $10^{th}$ GCD cycles).

**J. Complete electrochemical studies of Fe-RGO@SS (negative electrode):**

Prior to assemble the SHASC device, comprehensive electrochemical analysis of Fe-RGO@SS has been executed utilizing a three-electrode cell set-up within –1.0–0 V potential window in presence of aqueous 1 M KOH. Figure S6a illustrates the CV profile of Fe-RGO@SS at several scan rates of 2, 5, 10, 30, 50, 100, and 150 mV/s, individually. All the acquired CV profiles exhibits a near-rectangular nature (owing to the existence of RGO) associated with a pair of redox peaks (owing to the existence of $Fe_3O_4$ and minute $Fe_2O_3$). As can be recognized in Figure S6b, the anodic peak appears at – 0.58 V while the cathodic peak appears at – 0.89 V attributed to Fe (II) ↔Fe (III) redox pairs.[34] The shape of the CV curves deviates from ideal rectangular-type (EDLC behavior) suggesting the existence of both Faradaic and EDLC response. An electrostatic interaction between the electrolyte ions and RGO leads to physical adsorption and desorption of electrolyte ions at the electrolyte-RGO interfaces. In addition, improved electrolyte penetration ensures enhanced interaction between $Fe^{2+}/Fe^{3+}$ ions with $OH^-$ which eventually reflected by the improved electrochemical performance. Therefore, the electrode-electrolyte interactions have a direct effect on the capacitive and device performance. The GCD profiles of Fe-RGO@SS has been displayed in Figure S6c at a varying current density of 1, 2, 5, 10 and 20 A/g within –1.0–0 V. All the profiles likewise illustrate a combined electrochemical response. The Fe-RGO@SS reveals a $C_{sp}$ of ~ 385.0 F/g ($C_s \approx$ 106.95 mAh/g) at 1 A/g and a $C_A$ of ~ 4620 mF/cm$^2$ at an areal current density of 12 mA/cm$^2$. The actual mass of Fe-RGO on SS was ~ 0.048 g. The $C_{sp}$ still retains up to ~ 346.0 F/g ($C_s \approx$ 96.12 mAh/g) at a high current density of 20 A/g signifying admirable rate capability of Fe-RGO. Figure S6d shows the variation of gravimetric $C_{sp}$ values with the applied current density. A gentle diminution in the $C_{sp}$ values has been observed with the increment of current density. Figure S6e illustrates the variation of $C_A$ with the areal current density. As can be seen, the $C_A$ still retains up to ~ 4150 mF/cm$^2$ even at 240 mA/cm$^2$. Figure S6f depicts the Nyquist plot of Fe-RGO@SS electrode. Initially, it exhibits an $R_{ct}$ value of 2.42 Ω and $R_s$ of 0.6 Ω. The linear nature of

the profile at low frequency eventually illustrates enhanced diffusion of the electrolytic ions within the flake-type architecture of Fe-RGO. The stacked RGO flakes (with nanoscale separation) in Fe-RGO eventually afford enriched electrode-electrolyte interactions. Impressively, after 5000 GCD cycles, it exhibits an $R_{ct}$ value of ~ 2.63 Ω (small increase compared to initial $R_{ct}$) and $R_s$ of 0.6 Ω. Thus, the stability and integrity of stacked-like architectures of Fe-RGO even after 5000 GCD cycles can further be perceived. It is to be stated that during long and vigorous electrochemical cycling, the iron oxide NPs prevents coalescence of RGO flakes and provides suitable electrode-electrolyte interactions (as can be realized from similar $R_{ct}$). Also, the linear portion of the Nyquist plot after 5000 cycles at low frequency ascertains enhanced diffusion of the electrolytic ions within flake-type Fe-RGO after vigorous cycling. It also illustrates efficient "electrode-electrolyte interactions" persisting even after 5000 GCD cycles. Moreover, the Nyquist plot of pristine RGO@SS exhibits an increased $R_{ct}$ of 3.83 Ω and an $R_s$ value of 0.96 Ω. This could be due to instant coalescence of the adjacent stacked RGO flakes during measurements and restrict electrolyte penetration.

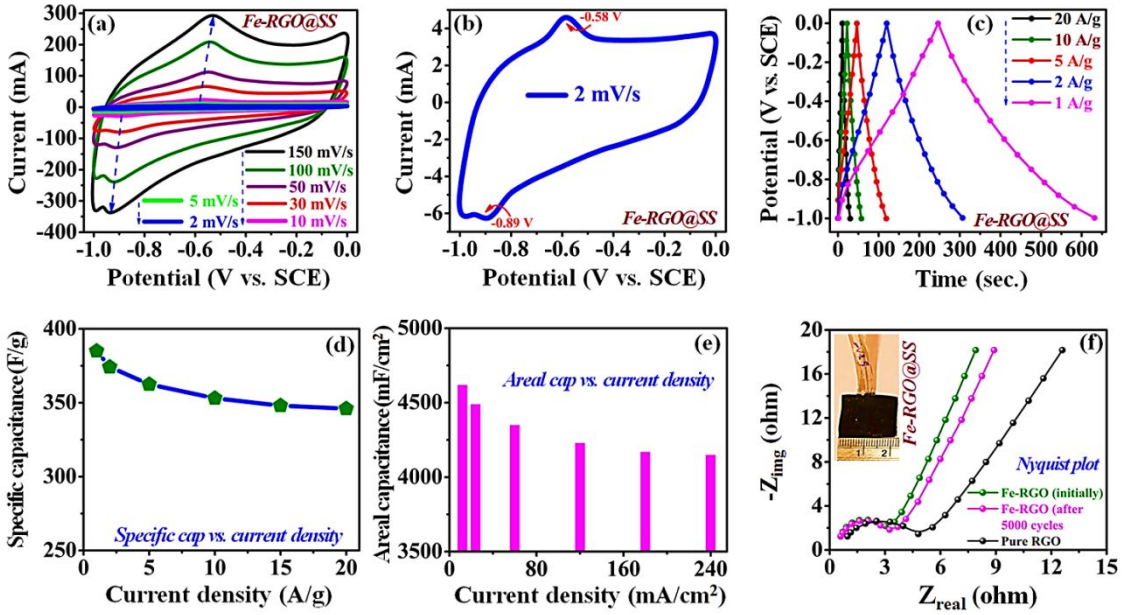


**Figure S6.** CV profiles of Fe-RGO@SS: (a) at different scan rates. (b) at 2 mV/s. (c) GCD profiles at several current densities. (d and e) Variation of $C_{sp}$ and $C_A$ values with the applied current densities, accordingly. (f) Nyquist plot. (Inset shows the photograph of Fe-RGO deposited SS fabric electrode).

**K. Estimation of the working potential range:**

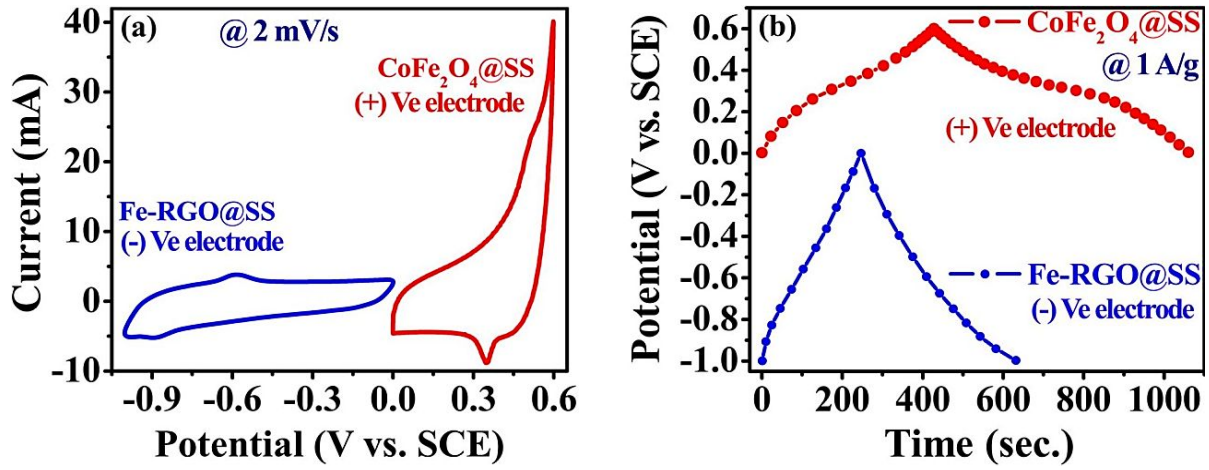


**Figure S7** (a) CV profiles of $CoFe_2O_4$@SS (+ Ve) and Fe-RGO@SS (–Ve) collectively at 2 mV/s. (b) Collective GCD profiles of the two component electrodes obtained at 1 A/g.

**Table S1: Comparison of $C_{sp}$, energy/power density and working voltage of our SHASC with other related outcomes already reported in the literatures:**

| Materials/Device | $C_{sp}$ (F/g) | Working voltage (V) | Energy density (Wh/Kg) | Power density (W/Kg) | Ref. |
|---|---|---|---|---|---|
| $ZnFe_2O_4$/NRG// $ZnFe_2O_4$/NRG | ~ 37.0 F/g (at 0.3 A/g) | 0–1.2 V | 6.7 | 3000 | 35 |
| $NiFe_2O_4$ (Three electrode system) | 454.0 (at 1 A/g) | 0–0.6 V | – | – | 36 |
| $MnCoFeO_4$ (Three electrode) | 670.0 (at 1.5 A/g) | 0–0.45 V | 3.15 | 2250 | 37 |
| $CoFe_2O_4$//RGO (Asymmetric) | 38.0 (at 3 mA/cm$^2$) | 0–1.5 V | 12.14 | 643.0 | 38 |
| $CoFe_2O_4$/C//AC (Asymmetric) | 160 (at 0.25 A/g) | 0–1.6 V | 14.38 | 720.0 | 33 |
| $CoFe_2O_4$@SS//Fe-RGO@SS (Asymmetric) | 155.8 (at 1 A/g) | 0–1.6 V | 55.4 (at 1 A/g) 46.5 (at 10 A/g) | 800.0 (at 1 A/g) 8000.0 (at 10 A/g) | This work |

**L. Mechanical durability and swelling ratio of the $Fe^{3+}$–PAA/KOH membrane/separator:**

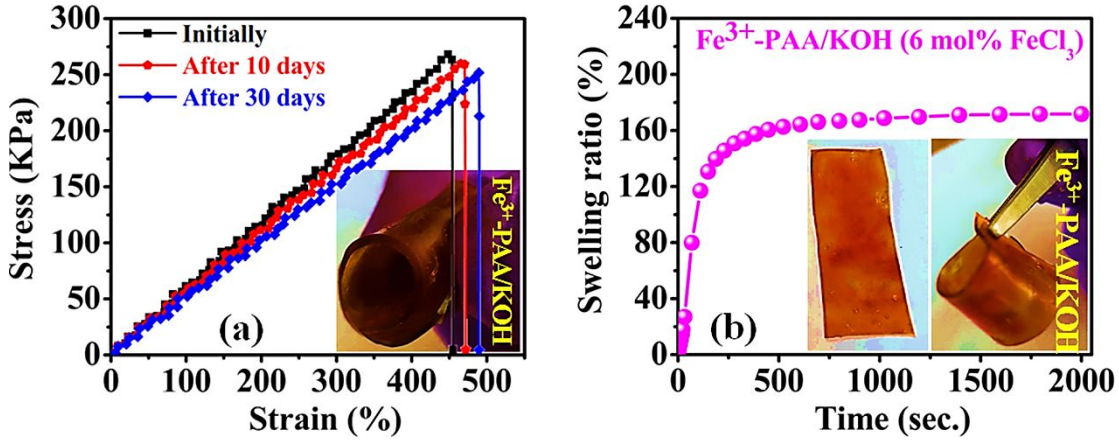


**Figure S8.** (a) Stress *vs.* strain curves of the KOH soaked $Fe^{3+}$–PAA membrane: Initially, after 10 and 30 consecutive days. (Inset portrays the photograph of a rolled KOH soaked $Fe^{3+}$–PAA membrane). (b) Swelling ratio (%) at several immersing time intervals (in 1 M aqueous KOH).

**M. Output performances of the TENG:**

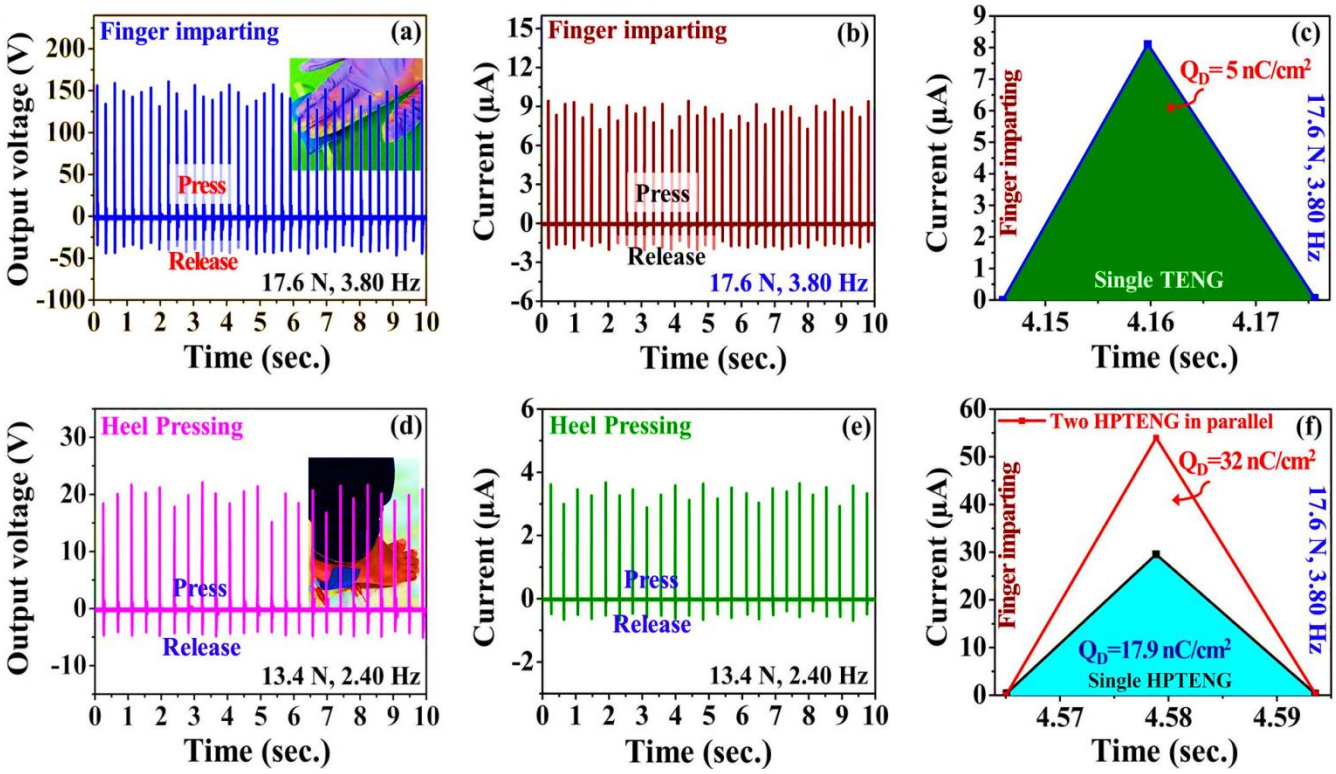


**Figure S9.** (a) $V_O$ of the TENG upon finger imparting. (Inset displays the photograph of finger imparting on TENG). (b) $I_{SC}$ generated by TENG upon finger imparting. (c) Calculation of SCD ($Q_D$)

from *i* vs. t profile of the TENG. (Coloured region resembles the integral area used to calculate $Q_D$). (d) $V_O$ of the TENG during heel pressing. (Inset shows the photograph of heel pressing on TENG). (e) $I_{SC}$ generated upon heel pressing. (f) Calculation of $Q_D$ from *i* vs. t curves for a single and two parallelly connected HPTENGs.

**N. Output performances of the HPTENG:**

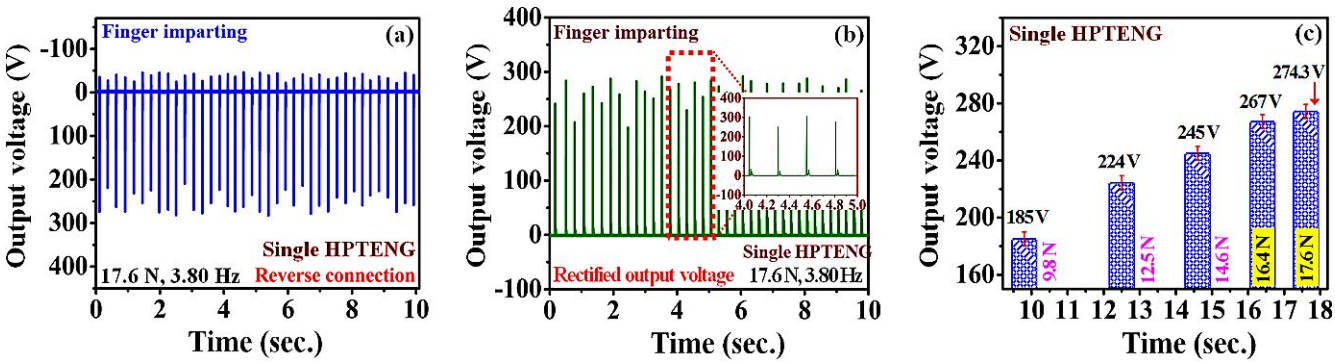


**Figure S10.** (a) $V_O$ generated by a single HPTENG in reverse connection. (b) Rectified $V_O$ signals generated by a single HPTENG under frequent finger imparting. (Inset depicts the magnified view). (c) Variation of the $V_O$ of single HPTENG with altering the magnitude of compressive force (at a constant f = 3.80 Hz).

**O. Working mechanism of the sandwich-type SCSHASC upon vertical contact-separation:**

Figure S11a demonstrates the complete schematic diagram of the sandwich-type SCSHASC power cell. As revealed previously, the device consists of a SHASC unit sandwiched between two parallelly connected HPTENGs. A full-wave bridge rectifier is introduced to mutually connect the SHASC and HPTENGs. Upon application of repetitive compressive force/stress on the top of the SCSHASC power cell, it harvests electrical energy and stores the energy (as electrochemical energy) for sustainable power supply (Figure S11b). The typical working mechanism of the assembled SCSHASC power cell upon vertical contact-separation is illustrated serially in Figure S11(c–f). At the initial stage, the constituent triboelectric friction layers (SS and PVDF–HFP/SS impregnated micro-patterned PDMS)

of individual HPTENGs do not contain any electric potential (Figure S11a). Owing to sandwich-type design, the +Ve and –Ve triboelectric friction layers will contact twice upon one-time compression.[39] When compressive force is applied on the top of the SCSHASC power cell (Figure S11c), the upper triboelectric friction layer (PVDF–HFP/SS impregnated PDMS) first comes in contact with the adjacent bottom SS fabric layer (components of HPTENG–1); followed by instant ejection of electrons from the SS surface. As a result, the bottom SS become positive and the upper composite film-strip gains negative charges on its surface (as per the triboelectric series). The potential difference generated between the two adjacent layers essentially drives the elections to charge the inner SHASC unit through a rectifier. Afterwards, the bottom triboelectric friction layer of HPTENG-2 (PVDF–HFP/SS impregnated PDMS) immediately touches its adjacent upper SS layer and thereby producing a current in the same direction (Figure S11d). The flow of current persists till the device attains an electrical equilibrium state. Owing to the inherent tendency of the compressed SCSHASC to recover its original sandwich-like structure, the separation distance between the friction layers of each HPTENG increases after the removal of applied force. Therefore, the generated charges create a reverse potential. Once the bottom friction layer of HPTENG-2 leaves its adjacent upper SS layer, positive charges are induced on the impregnated SS electrode of the bottom triboelectric film-strip (Figure S11e). As a result, the electrons flow through the external circuit in the reverse direction. Consequently, the top triboelectric film-strip of HPTENG-1 leaves its adjacent bottom SS layer (Figure S11f) causing the generation of output peak and the device attains equilibrium further. As can be realized, both the HPTENGs scavenge mechanical energy by a coupling of contact electrification and electrostatic induction. Before charging the internal SHASC, the alternating current (AC) harvested from each HPTENG has been rectified to direct current (DC) by a rectifier. Upon applying this generated DC on the constituent electrodes of the SHASC, it starts charging gently. Besides, the charging of the SHASC unit is governed by the ongoing electrochemical reactions. Initially, no potential is applied across the SHASC

electrodes and hence, no electrochemical reaction will occur. When electric potential is applied (during charging by the HPTENGs), the electrochemical equilibrium is hampered. This potential difference essentially drives the electrolytic ions ($K^+$ and $OH^-$) to the respective constituent electrodes through the pores of the hydrogel separator. As a result, the internal SHASC unit of the sandwich-type SCSHASC power cell stores charges gradually. Since, the inner supercapacitor reveals self-healing features, any unexpected damage/breakage of its components after numerous compression/stress cycles can be automatically repaired.

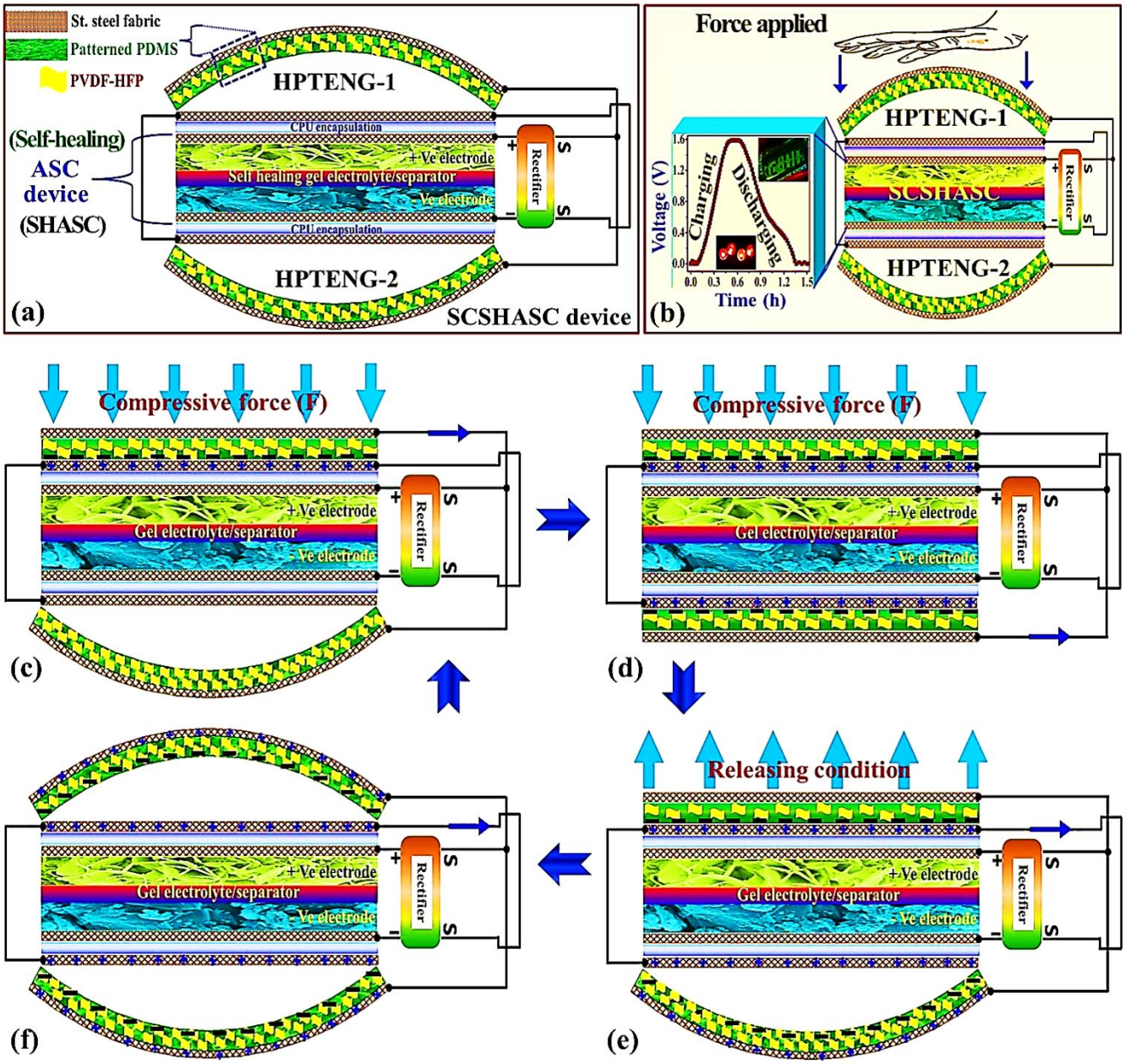

**Figure S11.** (a) Schematic diagram of the sandwich-type SCSHASC power cell (with two arc-shaped HPTENGs, one inner SHASC unit and a full wave bridge rectifier unit). (b) Effect of compressive force/mechanical deformation on the top of SCSHASC. (c–f) Schematic diagrams demonstrating the working mechanism of the SCSHASC: (c and d) under stressed conditions, (e) releasing condition, and (f) back to its original state/shape.

**P. GCD and EIS analysis of the SHASC component electrodes after repetitive imparting cycles:**

In order to support the microstructural stability of both $CoFe_2O_4$ (microflower) and Fe-RGO (stacked-flakes) against repetitive mechanical imparting/deformations, electrochemical measurements i.e. GCD and EIS of each component electrodes ($CoFe_2O_4$@SS and Fe-RGO@SS) has been executed after long and repetitive imparting cycles. GCD has been executed at 1 A/g to check any significant capacitance deterioration as a result of microstructural damage after repetitive imparting/deformation. Figure S12a and b represents the comparative GCD profiles of $CoFe_2O_4$@SS and Fe-RGO@SS (before and after repetitive imparting cycles), separately. It has been perceived that the specific capacitance and the areal capacitance remain virtually unaltered (a slight variation) before and after repetitive imparting/tapping cycles (for both the electrodes). EIS analysis has been executed to check any significant resistance or impedance deterioration as a result of microstructural damage after repetitive deformation. Figure S12c and d demonstrates the comparative EIS profiles of $CoFe_2O_4$@SS and Fe-RGO@SS (before and after repetitive imparting), separately. Likewise, the resistance characteristics ($R_s$ and $R_{ct}$) of the electrodes will remain almost unaltered (little variation) after long and repetitive imparting cycles (as compared to their initial $R_s$ and $R_{ct}$ values). Hence, the stability of the component electrodes ($CoFe_2O_4$@SS and Fe-RGO@SS) against long and repetitive imparting cycles can be confirmed both from morphological and electrochemical perspectives. The empirical values of $C_{sp}$, $C_A$, $R_s$ and $R_{ct}$ before and after repetitive imparting cycles are tabulated in Figure S12 e and f.

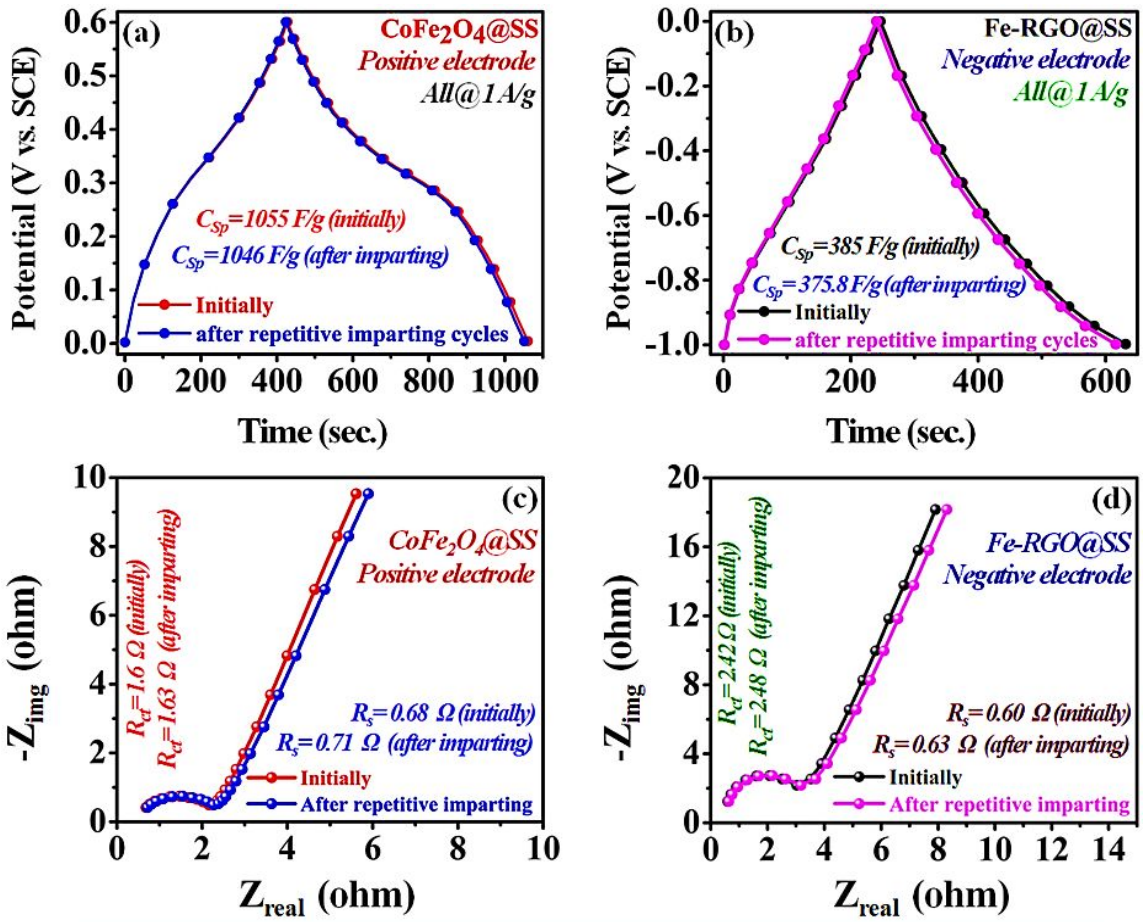


(e)

| *Electrodes* | *$C_{sp}$ (F/g) (Initially)* | *$C_{sp}$ (after repetitive imparting cycles)* | *$C_A$ (mF/cm²) (Initially)* | *$C_A$ (after repetitive imparting cycles)* |
|---|---|---|---|---|
| *$CoFe_2O_4$@SS* | 1055 F/g @ 1 A/g | 1046 F/g @ 1 A/g | 6850 mF/cm² @ 6.5 mA/cm² | 6797 mF/cm² @ 6.5 mA/cm² |
| *Fe-RGO@SS* | 385 F/g @ 1A/g | 375.8 F/g @ 1A/g | 4620 mF/cm² @ 12 mA/cm² | 4509 mF/cm²@ 12 mA/cm² |

(f)

| *Electrodes* | *$R_s$ (Ω) (Initially)* | *$R_s$ (Ω) (after repetitive imparting cycles)* | *$R_{ct}$ (Ω) (Initially)* | *$R_{ct}$ (Ω) (after repetitive imparting cycles cycles)* |
|---|---|---|---|---|
| *$CoFe_2O_4$@SS* | 0.68 | 0.71 | 1.60 | 1.63 |
| *Fe-RGO@SS* | 0.60 | 0.63 | 2.42 | 2.48 |

**Figure S12.** GCD profiles of (a) $CoFe_2O_4$@SS and (b) Fe-RGO@SS: before and after long-repetitive imparting cycles (at 1 A/g). Nyquist plots of (c) $CoFe_2O_4$@SS and (d) Fe-RGO@SS: before and after long-repetitive imparting cycles. The $C_{sp}$, $C_A$, $R_s$ and $R_{ct}$ values before and after long imparting cycles are tabulated in (e) and (f).

**Supporting Information Videos**

The characteristic self-charging and self-healing features revealed by the SCSHASC# power cell are demonstrated in three video clips (Supporting Video S1, S2 and S3) in Supporting Information Videos.

**REFERENCES**


(1) Sartale, S.; Lokhande, C.; Ganesan, V. Electrochemical Deposition and Characterization of $CoFe_2O_4$ Thin Films. *Phys. Status Solidi (a)* **2005,** *202*, 85–94.

(2) Hua, Z.; Chen, R.; Li, C.; Yang, S.; Lu, M.; Gu, B.; Du, Y. $CoFe_2O_4$ Nanowire Arrays Prepared by Template-Electrodeposition Method and Further Oxidization. *J. Alloys Compd.* **2007,** *427*, 199–203.

(3) Maitra, A.; Karan, S. K.; Paria, S.; Das, A. K.; Bera, R.; Halder, L.; Si, S. K.; Bera, A.; Khatua, B. B. Fast Charging Self-Powered Wearable and Flexible Asymmetric Supercapacitor Power Cell with Fish Swim Bladder as an Efficient Natural Bio-Piezoelectric Separator. *Nano Energy* **2017,** *40*, 633–645.

(4) Li, C.; Islam, M. M.; Moore, J.; Sleppy, J.; Morrison, C.; Konstantinov, K.; Dou, S. X.; Renduchintala, C.; Thomas, J. Wearable Energy-Smart Ribbons for Synchronous Energy Harvest and Storage. *Nat. Commun.* **2016**, *7*, 13319. [**DOI:** 10.1038/ncomms13319]

(5) Marcano, D. C.; Kosynkin, D. V.; Berlin, J. M.; Sinitskii, A.; Sun, Z.; Slesarev, A.; Alemany, L. B.; Lu, W.; Tour, J. M. Improved Synthesis of Graphene Oxide. *ACS Nano* **2010,** *4*, 4806–4814.

(6) Fan, Z.-J.; Kai, W.; Yan, J.; Wei, T.; Zhi, L.-J.; Feng, J.; Ren, Y.-m.; Song, L.-P.; Wei, F. Facile Synthesis of Graphene Nanosheets via Fe Reduction of Exfoliated Graphite Oxide. *ACS Nano* **2010,** *5*, 191–198.

(7) Bera, R.; Maitra, A.; Paria, S.; Karan, S. K.; Das, A. K.; Bera, A.; Si, S. K.; Halder, L.; De, A.; Khatua, B. B. An Approach to Widen the Electromagnetic Shielding Efficiency in PDMS/Ferrous Ferric Oxide Decorated RGO–SWCNH Composite Through Pressure Induced Tunability. *Chem. Eng. J.* **2018,** *335*, 501–509.

(8) Aphesteguy, J. C.; Jacobo, S. E. Composite of Polyaniline Containing Iron Oxides. *Phys. B* **2004,** *354*, 224–227.

(9) Ma, M.; Zhang, Y.; Guo, Z.; Gu, N. Facile Synthesis of Ultrathin Magnetic Iron Oxide Nanoplates by Schikorr Reaction. *Nanoscale Res. Lett.* **2013,** *8*, 1–7.

(10) Guo, Y.; Zhou, X.; Tang, Q.; Bao, H.; Wang, G.; Saha, P. A Self-Healable and Easily Recyclable Supramolecular Hydrogel Electrolyte for Flexible Supercapacitors. *J. Mater. Chem. A* **2016,** *4*, 8769–8776.

(11) Karan, S. K.; Mandal, D.; Khatua, B. B. Self-Powered Flexible Fe-Doped RGO/PVDF Nanocomposite: An Excellent Material for a Piezoelectric Energy Harvester. *Nanoscale* **2015,** *7*, 10655–10666.

(12) Khomenko, V.; Raymundo-Pinero, E.; Béguin, F. Optimisation of an Asymmetric Manganese Oxide/Activated Carbon Capacitor Working at 2V in Aqueous Medium. *J. Power Sources* **2006,** *153*, 183–190.

(13) Kim, J.-H.; Lee, Y.-S.; Sharma, A. K.; Liu, C. G. Polypyrrole/Carbon Composite Electrode for High-Power Electrochemical Capacitors. *Electrochim. Acta* **2006,** *52*, 1727–1732.

(14) Yan, J.; Fan, Z.; Sun, W.; Ning, G.; Wei, T.; Zhang, Q.; Zhang, R.; Zhi, L.; Wei, F. Advanced Asymmetric Supercapacitors Based on $Ni(OH)_2$/Graphene and Porous Graphene Electrodes with High Energy Density. *Adv. Funct. Mater.* **2012,** *22*, 2632–2641.

(15) Hou, C.; Huang, T.; Wang, H.; Yu, H.; Zhang, Q.; Li, Y. A Strong and Stretchable Self-Healing Film with Self-activated Pressure Sensitivity for Potential Artificial Skin Applications. *Sci. Rep.* **2013,** *3*, 3138. [**DOI:** 10.1038/srep03138]

(16) Maiti, S.; Karan, S. K.; Lee, J.; Mishra, A. K.; Khatua, B. B.; Kim, J. K. Bio-Waste Onion Skin as an Innovative Nature-Driven Piezoelectric Material with High Energy Conversion Efficiency. *Nano Energy* **2017,** *42*, 282–293.

(17) Paria, S.; Karan, S. K.; Bera, R.; Das, A. K.; Maitra, A.; Khatua, B. B. A Facile Approach To Develop a Highly Stretchable PVC/$ZnSnO_3$ Piezoelectric Nanogenerator with High Output Power Generation for Powering Portable Electronic Devices. *Ind. Eng. Chem. Res.* **2016,** *55*, 10671–10680.

(18) Jung, W.-S.; Kang, M.-G.; Moon, H. G.; Baek, S.-H.; Yoon, S.-J.; Wang, Z.-L.; Kim, S.-W.; Kang, C.-Y. High Output Piezo/Triboelectric Hybrid Generator. *Sci. Rep.* **2015,** *5*, 9309. [**DOI:** 10.1038/srep09309]

(19) Han, F.; Ma, L.; Sun, Q.; Lei, C.; Lu, A. Rationally Designed Carbon-Coated $Fe_3O_4$ Coaxial Nanotubes with Hierarchical Porosity as High-Rate Anodes for Lithium Ion Batteries. *Nano Res.* **2014,** *7*, 1706–1717.

(20) Fujii, T. d.; De Groot, F.; Sawatzky, G.; Voogt, F.; Hibma, T.; Okada, K. *In-situ* XPS Analysis of Various Iron Oxide Films Grown by $NO_2$-Assisted Molecular-Beam Epitaxy. *Phys. Rev. B* **1999,** *59*, 3195–3202.

(21) Wang, R.; Xu, C.; Sun, J.; Gao, L. Three-Dimensional $Fe_2O_3$ Nanocubes/Nitrogen-Doped Graphene Aerogels: Nucleation Mechanism and Lithium Storage Properties. *Sci. Rep.* **2014,** *4*, 7171. [**DOI:** 10.1038/srep07171]

(22) Maitra, A.; Das, A. K.; Bera, R.; Karan, S. K.; Paria, S.; Si, S. K.; Khatua, B. B. An Approach to Fabricate PDMS Encapsulated All-Solid-State Advanced Asymmetric Supercapacitor Device with Vertically Aligned Hierarchical Zn–Fe–Co Ternary Oxide Nanowire and Nitrogen Doped Graphene Nanosheet for High Power Device Applications. *ACS Appl. Mater. Interfaces* **2017,** *9*, 5947–5958.

(23) Muralikrishna, S.; Sureshkumar, K.; Varley, T. S.; Nagaraju, D. H.; Ramakrishnappa, T. *In-situ* Reduction and Functionalization of Graphene Oxide with L-Cysteine for Simultaneous Electrochemical Determination of Cadmium (II), Lead (II), Copper (II), and Mercury (II) Ions. *Anal. Methods* **2014,** *6*, 8698–8705.

(24) Bohara, R. A.; Thorat, N. D.; Yadav, H. M.; Pawar, S. H. One-Step Synthesis of Uniform and Biocompatible Amine Functionalized Cobalt Ferrite Nanoparticles: A Potential Carrier for Biomedical Applications. *New J. Chem.* **2014,** *38*, 2979–2986.

(25) Allaedini, G.; Tasirin, S. M.; Aminayi, P. Magnetic Properties of Cobalt Ferrite Synthesized by Hydrothermal Method. *Int. Nano Lett.* **2015,** *5*, 183–186.

(26) Dong, Y.-l.; Zhang, X.-f.; Cheng, X.-l.; Xu, Y.-m.; Gao, S.; Zhao, H.; Huo, L.-h. Highly Selective $NO_2$ Sensor at Room Temperature Based on Nanocomposites of Hierarchical Nanosphere-like α-$Fe_2O_3$ and Reduced Graphene Oxide. *RSC Adv.* **2014,** *4*, 57493–57500.

(27) Wang, N.; Hu, B.; Chen, M.-L.; Wang, J.-H. Polyethylenimine Mediated Silver Nanoparticle-Decorated Magnetic Graphene as a Promising Photothermal Antibacterial Agent. *Nanotechnol.* **2015,** *26*, 195703. [**DOI:** 10.1088/0957-4484/26/19/195703]

(28) Zhu, S.; Guo, J.; Dong, J.; Cui, Z.; Lu, T.; Zhu, C.; Zhang, D.; Ma, J. Sonochemical Fabrication of $Fe_3O_4$ Nanoparticles on Reduced Graphene Oxide for Biosensors. *Ultrason. Sonochem.* **2013,** *20*, 872–880.

(29) Murugesan, C.; Chandrasekaran, G. Impact of $Gd^{3+}$ Substitution on the Structural, Magnetic and Electrical Properties of Cobalt Ferrite Nanoparticles. *RSC Adv.* **2015,** *5*, 73714–73725.

(30) Peik-See, T.; Pandikumar, A.; Ngee, L. H.; Ming, H. N.; Hua, C. C. Magnetically Separable Reduced Graphene Oxide/Iron Oxide Nanocomposite Materials for Environmental Remediation. *Catal. Sci. Technol.* **2014,** *4*, 4396–4405.

(31) Wang, T.; Li, Y.; Wang, L.; Liu, C.; Geng, S.; Jia, X.; Yang, F.; Zhang, L.; Liu, L.; You, B. Synthesis of Graphene/α-$Fe_2O_3$ Composites with Excellent Electromagnetic Wave Absorption Properties. *RSC Adv.* **2015,** *5*, 60114–60120.

(32) Cherian, C. T.; Sundaramurthy, J.; Kalaivani, M.; Ragupathy, P.; Kumar, P. S.; Thavasi, V.; Reddy, M.; Sow, C. H.; Mhaisalkar, S. G.; Ramakrishna, S. Electrospun α-$Fe_2O_3$ Nanorods as a Stable, High Capacity Anode Material for Li-Ion Batteries. *J. Mater. Chem.* **2012,** *22*, 12198–12204.

(33) Zhao, Y.; Xu, Y.; Zeng, J.; Kong, B.; Geng, X.; Li, D.; Gao, X.; Liang, K.; Xu, L.; Lian, J. Low-Crystalline Mesoporous $CoFe_2O_4$/C Composite with Oxygen Vacancies for High Energy Density Asymmetric Supercapacitors. *RSC Adv.* **2017,** *7*, 55513–55522.

(34) Wang, Q.; Jiao, L.; Du, H.; Wang, Y.; Yuan, H. $Fe_3O_4$ Nanoparticles Grown on Graphene as Advanced Electrode Materials for Supercapacitors. *J. Power Sources* **2014,** *245*, 101–106.

(35) Li, L.; Bi, H.; Gai, S.; He, F.; Gao, P.; Dai, Y.; Zhang, X.; Yang, D.; Zhang, M.; Yang, P. Uniformly Dispersed $ZnFe_2O_4$ Nanoparticles on Nitrogen-Modified Graphene for High-Performance Supercapacitor as Electrode. *Sci. Rep.* **2017,** *7*, 43116. [**DOI:** 10.1038/srep43116]

(36) Dong, B.; Li, M.; Xiao, C.; Ding, D.; Gao, G.; Ding, S. Tunable Growth of Perpendicular Cobalt Ferrite Nanosheets on Reduced Graphene Oxide for Energy Storage. *Nanotechnol.* **2016,** *28*, 055401.[**DOI:** 10.1088/1361-6528/28/5/055401]

(37) Elkholy, A. E.; Heakal, F. E.-T.; Allam, N. K. Nanostructured Spinel Manganese Cobalt Ferrite for High-Performance Supercapacitors. *RSC Adv.* **2017,** *7*, 51888–51895.

(38) Sankar, K. V.; Selvan, R. K.; Meyrick, D. Electrochemical Performances of $CoFe_2O_4$ Nanoparticles and a rGO Based Asymmetric Supercapacitor. *RSC Adv.* **2015,** *5*, 99959–99967.

(39) Song, Y.; Cheng, X.; Chen, H.; Huang, J.; Chen, X.; Han, M.; Su, Z.; Meng, B.; Song, Z.; Zhang, H. Integrated Self-Charging Power Unit with Flexible Supercapacitor and Triboelectric Nanogenerator. *J. Mater. Chem. A* **2016,** *4*, 14298–14306.